Lawrence Berkeley National Laboratory
Recent Work

Title

Metal-oxygen decoordination stabilizes anion redox in Li-rich oxides.

Permalink

Journal

ISSN

Authors

Hong, Jihyun
Gent, William E
Xiao, Penghao
et al.

Publication Date

DOI

Peer reviewed

Metal-Oxygen Decoordination Stabilizes Anion Redox in Li-rich Oxides

Authors: Jihyun Hong[1,2,3,4§,†], William E. Gent[5,6†], Penghao Xiao[7], Kipil Lim[1,2,3,4], Dong-Hwa Seo[8], Jinpeng Wu[3,6], Peter M. Csernica[1], Christopher J. Takacs[2], Dennis Nordlund[2], Cheng-Jun Sun[9], Kevin H. Stone[2], Donata Passarello[2], Wanli Yang[6], David Prendergast[10], Gerbrand Ceder[7,8]*, Michael F. Toney[2,4]*, William C. Chueh[1,3,4]*

Affiliations:

[1] Department of Materials Science and Engineering, Stanford University, 496 Lomita Mall, Stanford, CA 94305, U.S.A.

[2] Stanford Synchrotron Radiation Lightsource, SLAC National Accelerator Laboratory, 2575 Sand Hill Road, Menlo Park, CA 94025, U.S.A.

[3] Stanford Institute for Materials & Energy Sciences, SLAC National Accelerator Laboratory, 2575 Sand Hill Road, Menlo Park, CA 94025, U.S.A.

[4] Applied Energy Division, SLAC National Accelerator Laboratory, 2575 Sand Hill Road, Menlo Park, CA 94025, U.S.A.

[5] Department of Chemistry, Stanford University, 333 Campus Drive, Stanford, CA 94305, U.S.A.

[6] The Advanced Light Source, Lawrence Berkeley National Laboratory, 1 Cyclotron Road, Berkeley, CA 94720 U.S.A.

[7] Materials Sciences Division, Lawrence Berkeley National Laboratory, 1 Cyclotron Road, Berkeley, CA 94720, U.S.A.

[8] Department of Materials Science and Engineering, University of California, Berkeley, 2607 Hearst Ave, Berkeley, CA 94720, U.S.A.

[9] The Advanced Photon Source, Argonne National Laboratory, 9700 Cass Ave, Lemont, IL 60439, U.S.A.

[10] The Molecular Foundry, Lawrence Berkeley National Laboratory, 1 Cyclotron Road, Berkeley, CA 94720, U.S.A.

§ Present address: High-Temperature Energy Materials Research Center, Korea Institute of Science and Technology (KIST), Seoul, 02792, Republic of Korea.

* Correspondence to: gceder@berkeley.edu, wchueh@stanford.edu, mftoney@slac.stanford.edu

† Equal contribution authors.

33   **Abstract**:

34   Reversible high voltage redox chemistry is an essential component of many electrochemical

35   technologies, from (electro)catalysts to lithium-ion batteries. Oxygen anion redox has garnered

36   intense interest for such applications, particularly lithium ion batteries, as it offers substantial

37   redox capacity at > 4 V vs. Li/Li$^+$ in a variety of oxide materials. However, oxidation of oxygen

38   is almost universally correlated with irreversible local structural transformations, voltage

39   hysteresis, and voltage fade, which currently preclude its widespread use. By comprehensively

40   studying the Li$_{2-x}$Ir$_{1-y}$Sn$_y$O$_3$ model system, which exhibits tunable oxidation state and structural

41   evolution with y upon cycling, we reveal that this structure-redox coupling arises from the local

42   stabilization of short ~ 1.8 Å metal-oxygen π bonds and ~ 1.4 Å O–O dimers during oxygen

43   redox, which occurs in Li$_{2-x}$Ir$_{1-y}$Sn$_y$O$_3$ through ligand-to-metal charge transfer. Crucially,

44   formation of these oxidized oxygen species necessitates the decoordination of oxygen to a single

45   covalent bonding partner through formation of vacancies at neighboring cation sites, driving

46   cation disorder. These insights establish a point defect explanation for why anion redox often

47   occurs alongside local structural disordering and voltage hysteresis during cycling. Our findings

48   offer an explanation for the unique electrochemical properties of lithium-rich layered oxides,

49   with implications generally for the design of materials employing oxygen redox chemistry.

50

Main Text:

Reversible redox chemistry in solids under highly oxidizing conditions (e.g. vs H_2/H^+, Li/Li^+, or O_2) is a powerful tool in (electro)chemical systems, increasing the catalytic activity of oxygen-evolution and methane-functionalization (electro)catalysts as well as the energy and power densities of lithium-ion batteries (LIBs).[1] In LIBs in particular, employing high-voltage redox has been identified as a promising avenue to meeting the energy density demands of next-generation technologies such as plug-in electric vehicles.

Recently, anionic oxygen redox has been shown to offer access to substantial high-voltage (de)intercalation capacity in a range of electrode materials,[2-7] spurring an intense research effort to understand this phenomenon. While many oxygen-redox-active materials have been developed, they almost universally exhibit a host of irreversible electrochemical behaviors such as voltage hysteresis and voltage fade.[8] This is most notable in the anion-redox-active Li-rich layered oxides, $Li_{1+x}M_{1-x}O_2$ (M = a transition metal (TM) or non-transition metal such as Al, Sn, Mg, etc.), which exhibit capacities approaching 300 mAh g^{-1} but have yet to achieve commercial success due to such electrochemical behaviors.[5, 9] It has been shown both experimentally[10-12] and from first-principles thermodynamics[13] that the migration of M into empty Li sites[9] – creating structural disorder in the form of M_{Li}/V_M antisite/cation vacancy point defect pairs – is at the root of voltage profile evolution and depression, particularly during the first cycle. Oxygen redox has separately been shown to trigger voltage hysteresis and sluggish kinetics,[8, 14] with the implication being that oxygen redox and transition metal (TM) migration/vacancy formation are often intrinsically linked. Indeed, the coupling between oxygen redox, cation migration, and voltage hysteresis was recently observed.[6] However, under the two primary models that have emerged to describe the nature of the lattice oxygen in these materials (either a ~ 2.5 Å peroxo-like O_2^{n-}

3

74 dimer[3, 15] or an isolated O$^-$ anion[4, 5, 16]), it is unclear as to why the oxidation of oxygen should

75 lead to the correlated structural transformations and voltage hysteresis. It has been argued

76 qualitatively that the oxidation of oxygen destabilizes the layered structure;[2, 15] however, a robust

77 understanding of the materials design criteria for achieving structurally and electrochemically

78 reversible anion redox remains elusive.

79 In approaching this issue, we turn to layered Li_2IrO_3 (equivalently, $Li[Li_{0.33}Ir_{0.67}]O_2$ or LIO)

80 which is reported to exhibit anion redox, yet, unlike other Li-rich layered oxides, exhibits highly

81 reversible structural and electrochemical behavior during cycling.[15, 17] Upon substituting redox-

82 inactive Sn for Ir, the solid solution material $Li_2Ir_{1-y}Sn_yO_3$ (LISO) forms M_{Li}/V_M defects during

83 charge, accompanied by voltage hysteresis during subsequent cycling that is typical of other

84 anion-redox-active oxides.[15] This tunability makes LIO/LISO an ideal model system for studying

85 the link between anion redox, local structure, and irreversible electrochemistry.

86 In this work, we show that the difference in electrochemical and structural behavior between LIO

87 and LISO holds the key to understanding anion redox. Using a combination of bulk-sensitive

88 spectroscopic and structural probes in conjunction with first principles calculations, we

89 demonstrate that anion redox only occurs simultaneously with structural disordering (i.e.

90 antisite/vacancy formation) in LISO, and is completely absent in LIO up to 4.6 V, further

91 establishing the strong coupling between these two phenomena. We demonstrate that the ~ 2.5 Å

92 O–O dimers that form in LIO do not constitute oxidized oxygen, and that the high degree of

93 covalency and the low voltage of the Ir redox states together prevent oxygen redox from being

94 accessed in LIO. Crucially, we reveal the origin of the coupling between structural evolution and

95 oxygen redox in LISO using density-functional theory (DFT) calculations, wherein the low

96 valence electron count in delithiated LISO promotes charge transfer from O to Ir (essentially,

97   oxygen oxidation *via* ligand to metal charge transfer, or LMCT) through drastic changes in the

98   local bonding configuration. We identify two main bonding configurations that are able to

99   stabilize both the low valence electron count through LMCT and the resulting oxidized oxygen

100   species: short ~ 1.8 Å Ir-O π bonds (equivalently, terminal Ir=O oxo species) and short ~ 1.4 Å

101   O–O dimers. Both configurations require the decoordination of oxygen down to a single covalent

102   bonding partner, which is realized in the layered structure through vacancy formation due to in-

103   plane and out-of-plane site disorder (cation migration). Meanwhile, the higher valence electron

104   count in LIO disfavors LMCT and thus LIO exhibits minimal structural disordering, cation redox

105   only, and more reversible electrochemistry. While further investigation is needed to understand

106   how this mechanism depends on the nature of the TM, this point defect model can offer a causal

107   explanation for the nearly universal observation of structural and electrochemical irreversibility

108   in anion-redox-active Li-rich materials and reveals previously unconsidered design parameters

109   through which to improve them, such as the electronic and structural mechanism of LMCT and

110   oxygen decoordination. These principles apply generally to the design of the broad class of

111   highly oxidized oxides where anion redox is likely to play a role.

112

113   **Electrochemistry and phase behavior of Li$_2$IrO$_3$**

114   As previously reported,[15, 17] Fig. 1a shows that LIO exhibits two well-defined voltage plateaus

115   with average potentials of 3.45 V and 4.15 V versus Li/Li$^+$ and a total capacity of 1.5e$^-$ per Ir. It

116   was previously shown that LIO exhibits a layered structure with monoclinic *C2/m* symmetry,

117   with the Li and TMs in the TM layers ordered into a honeycomb-like arrangement, and

118   accommodates delithiation through changes in the stacking of the TM layers, changing from

119   initially O3 to O1[18] at the end of charge. This is further supported here by Rietveld refinement of

120   the synchrotron X-ray diffraction (XRD) patterns (figs. S1 & S2, tables S1 & S2, and

121   Supplementary discussion S1). In addition, we identify the intermediate Li_1IrO_3 phase as

122   exhibiting T3 stacking using DFT (Fig. S3). We note that the material studied here exhibits a

123   high degree of initial structural ordering and electrochemical reversibility, and is therefore more

124   similar to that reported by Kobayashi et al.[17] than McCalla et al.[15]

125   While it was previously shown that LIO exhibits minimal structural disordering during the first

126   charge, for this study it is important to quantify the cation vacancy/antisite formation during

127   electrochemical cycling such that it can be compared to LISO. We employed an iterative

128   approach to simultaneously refine the in-plane and out-of-plane site disorder as described in

129   Supplementary discussion S1 and Fig. S4. This approach eliminates the difficulty in site

130   occupancy determination resulting from the presence of stacking faults. We confirm the absence

131   of V_{Ir}/Ir_{Li} defects ($\leq 0.1\pm0.2\%$ of all Li sites occupied by Ir) in the discharged state both before

132   and after the first electrochemical cycle. In-plane site occupancy refinement of the fully charged

133   O1 structure is challenging due to distortions to the oxygen sublattice[15] and the absence of

134   superstructure peaks. However, out-of-plane refinement shows negligible Ir occupancy in the Li

135   layer in the fully charged state. Consistently, DFT calculations indicate that in-plane and out-of-

136   plane Ir antisite/vacancy defect pairs in the fully charged state have a positive formation energy

137   of +0.49 and +0.20 eV (per $Li_4Ir_8O_{24}$ supercell), respectively. Together, these results show why

138   LIO exhibits reversible electrochemistry: minimal cation disordering occurs during cycling. This

139   is unlike most other Li-rich materials in which anion redox is reported to occur.[7, 9, 12, 19]

140

141   **Multivalent iridium redox in Li_2IrO_3**

142   The nature of anion redox in LIO should therefore be examined with further scrutiny. In

143   addition, a strict definition of anion redox is needed. Until now, oxygen redox has been defined

144   as the depopulation of non-bonding (or "weakly/minimally hybridized") oxygen 2p states[5, 6, 16, 20,

145   21]. However, this definition does not take into account how materials respond to the depopulation

146   of these states, which as we will show later is a crucial component of oxygen redox. So, we

147   provide a more specific definition here: oxygen redox requires the depopulation of non-bonding

148   (or "weakly/minimally hybridized") oxygen *2p* states wherein the resulting holes reside in

149   predominantly oxygen character orbitals after any structural and electronic reorganization has

150   occurred. A previous study reported anion redox in LIO based on: (a) surface-sensitive X-ray

151   photoelectron spectroscopy (XPS) showing the appearance of an oxygen state with reduced

152   electron density, and (b) neutron diffraction and transmission electron microscopy (TEM)

153   measurements showing the contraction of the octahedral O–O distance from ~2.7 Å to ~2.5 Å.[15]

154   Here we use bulk-sensitive X-ray spectroscopic techniques to directly determine the nature of the

155   hole states formed during charge and, by induction, the redox processes in LIO. We first show in

156   Fig. 1 analysis of the *operando* transmission X-ray absorption near edge structure (XANES) at

157   the Ir L_3 edge during the first cycle of LIO.[19, 22, 23] Figure 1b shows that the white line (WL)

158   energy increases linearly during the galvanostatic charge up to $Li_{0.5}IrO_3$ and then decreases

159   linearly on discharge, nearly returning to its original value after the full cycle. Figure 1c,

160   meanwhile, shows that the WL intensity increases up to Li_1IrO_3 but then decreases when

161   charging further to $Li_{0.5}IrO_3$, with the trend reversing on discharge. Principal component analysis

162   and non-negative matrix factorization (NMF) of the XANES spectra (Supplementary discussion

163   S2 and Fig. S5) reveal the presence of three spectral end members corresponding to the Li_2IrO_3,

164   Li_1IrO_3, and $Li_{0.5}IrO_3$ compositions, consistent with the presence of two isosbestic points. These

165　three end member spectra (Fig. 1d, inset) reflect the observed changes, with $Li_{0.5}IrO_3$ having the

166　highest WL energy followed by Li_1IrO_3 and Li_2IrO_3, and with Li_1IrO_3 having the strongest WL

167　peak intensity. A linear combination analysis (LCA) using these end members confirms that the

168　entire spectral evolution is well described by two consecutive two-phase reactions between

169　Li_2IrO_3 and Li_1IrO_3, and between Li_1IrO_3 and $Li_{0.5}IrO_3$ (figs. 1d and S5).

170　To understand what these spectral changes indicate, we note that the L_3 WL energy has been

171　shown to vary linearly with formal Ir oxidation state.[34] Thus the linear trend during galvanostatic

172　cycling indicates a linear, monotonic change in Ir oxidation state, with a total WL shift of 1.2 eV.

173　The Ir WL energy difference between Ir^{6+} and Ir^{4+} compounds is typically between 1.4-2.0 eV,[23,

174　24] and the WL shift here is therefore consistent with Ir being oxidized by between 1.2-1.7 e^-.

175　Although it was argued that a loss in WL intensity indicates Ir reduction in Li_3IrO_4,[19] it has been

176　shown that the WL intensity of Ir^{6+} is lower than that of Ir^{5+},[23, 24] which may be due to the WL

177　intensity becoming dominated by relaxation quenching rather than d count for d counts below d^4-

178　d^5.[25] Thus both the WL energy and intensity suggest a monotonic oxidation of Ir from 4+ to

179　between 5.2+ and 5.7+.

180　Since the linear coefficient between WL energy and oxidation state appears to vary slightly

181　between materials,[23, 24] it is impossible to precisely quantify the final Ir oxidation state based on

182　XANES studies in other materials. Thus, although the monotonicity of the Ir oxidation is already

183　in striking contrast to the behavior of most anion redox active Li-rich oxides, whose TM ions

184　either stop being oxidized or are even reduced during the high voltage plateau,[4, 6, 16] and suggests

185　the absence of anion redox in LIO and a final Ir oxidation state of 5.5+, this cannot be proven

186　with XANES alone. To directly assess the contribution of bulk O to the LIO redox mechanism,

187　we perform soft X-ray absorption spectroscopy (sXAS) at the O K edge. Transmission and

188   fluorescence yield (FY) detection modes with probing depths of hundreds of nm were employed

189   (see methods). Figure 2a shows the O K edge sXAS-FY and transmission sXAS spectra of LIO

190   (initially in the $t_{2g}^{5}e_{g}^{0}$ electronic configuration) during the first electrochemical cycle. The peaks

191   at ~529 eV and 532 eV are ascribed to the unoccupied Ir $5d$-O $2p$ t_{2g} and e_{g}^{*} hybridized states,

192   respectively.[26, 27] The difference plots taken between different states of charge (Fig. 2b) clearly

193   show that the intensity of the t_{2g} peak increases and decreases throughout charge and discharge,

194   mirroring the evolution of the Ir L_3 WL (Fig. 1c). Figure 2c shows that the integrated area ratio

195   of the two O K XAS pre-edge peaks follows the same trend in transmission sXAS, which probes

196   the entirety of the particles, confirming that this is a bulk phenomenon.

197   The correlated changes at the O K and Ir L_3 edges indicate redox of a hybridized Ir–O state, and

198   are widely accepted as a fingerprint of conventional "TM–O" cation redox[6] observed in a variety

199   of compounds such as $LiNi_{0.5}Mn_{1.5}O_4$,[28] $LiFePO_4$,[29] *3d* layered TM oxides.[6, 26] While in these

200   systems the oxidation of the TM is accompanied by charge sharing with the anions, this clearly

201   does not qualify as oxygen redox according to the earlier definition since no *additional*

202   unhybridized O *2p* electrons are depopulated beyond the hybridized TM–O states. This is further

203   supported by resonant inelastic X-ray scattering (RIXS) at the O K edge. It has recently been

204   shown that depopulation of unhybridized O *2p* states in some Li-rich materials results in a sharp

205   absorption feature at ~ 530.8 eV excitation energy at the O K edge with a characteristic emission

206   at ~ 523.0 eV, evident in both RIXS maps[6] and single-energy RIXS spectra,[6, 16, 30, 31] which is

207   distinct from the energy of typical hybridization features in most TM oxides. Figure 2d shows,

208   however, that no such feature appears even in the fully charged LIO. Thus, in conjunction with

209   the XANES results, O K edge sXAS and RIXS further support pure multivalent, hybridized Ir–O

210   redox in the absence of oxygen redox in LIO.

211   This is also supported by DFT calculations. The predicted projected density of states (pDOS) of

212   the oxygen $2p$ and Ir $5d$ states of the three structures formed during cycling are shown in Fig. 2e.

213   Changes in the Ir and O pDOS as a function of Li stoichiometry show that all states depopulated

214   during delithiation contain both Ir and O character. The unhybridized O $2p$ states (*i.e.*, the non-

215   bonding (NB) O $2p$ band) lie ~ 2 eV below the Fermi level in $Li_{0.5}IrO_3$ and are therefore not

216   emptied. Insets in Fig. 2e plot the isosurface of the spin density of the lowest unoccupied (*i.e.*,

217   redox active) states around Ir and O for Li_1IrO_3 and $Li_{0.5}IrO_3$. (equivalent to 0.5 electrons per

218   formula unit, shaded in the DOS). In both cases, we observe large spin density around both Ir

219   and O ions in the shape of two distinct hybridized Ir $5d$-O $2p$ t_{2g} orbitals – likely d_{xy} and mixed

220   d_{yz}-d_{xz}. Thus, although all oxygen ions in LIO exhibit the linear Li–O–Li structural motif that

221   was recently shown to raise the energy of the O $2p$ states and promote oxygen redox in many Li-

222   rich materials (see Fig. S6),[5, 6, 32] these results demonstrate that the $Ir^{4/5.5+}$ redox band (where 5.5

223   denotes the average formal oxidation state) is too high in energy for these labile O $2p$ states to

224   compete for redox in LIO, similar to predictions made for V, Cr, and Mo.[5]

225   Having employed a suite of bulk-sensitive spectroscopic probes and computation, we show that

226   only hybridized TM–O states are accessed in LIO, with Ir reaching the 5.5+ formal oxidation

227   state at the end of charge. We therefore re-classify LIO as anion-redox inactive within the 2.5-4.6

228   V window. In terms of addressing previous conflicting conclusions, it is likely that the oxidized

229   oxygen species observed by XPS are due to near-surface phenomena which do not play a

230   significant role in the bulk redox mechanism. As for the long ~ 2.5 Å O–O dimers that were

231   observed to form in the bulk of charged LIO, we conclude that these species are not sufficient

232   evidence of oxidized oxygen. This is based on the observation that most TM-coordinated

233   oxidized oxygen dimers are between 1.3-1.5 Å in length.[33] We speculate on alternative

234   explanations for the dimerization phenomenon in Supplementary discussion S3 and Fig. S7.

235

236   **Extra capacity beyond Ir$^{5.5+}$ in LISO and irreversible electrochemical/structural evolution**

237   When Sn is substituted into Li_2IrO_3 to make solid-solution phase $Li_2Ir_{1-y}Sn_yO_3$, the

238   electrochemistry changes dramatically and becomes typical of that of anion redox active

239   materials (Fig. 3a). We use the notation LISO## to represent the compound with ## % Sn

240   content, and the term "LISO" to refer to the Sn-substituted materials generally. Regardless of Sn

241   content, when charged beyond Ir$^{5.5+}$, LISO exhibits a new plateau at ~ 4.35 V, followed by a

242   large voltage drop on the subsequent discharge, a permanently sloped voltage profile, and

243   voltage hysteresis that persists even at open circuit (Fig. S8). Despite the drastic changes to the

244   voltage profile, LISO25 exhibits reasonable capacity retention with cycling (74.5% after 192

245   cycles, Fig. S9). The new high voltage plateau, in conjunction with the additional reversible

246   capacity well beyond 1.5 e$^-$ per Ir (Fig. 3a), indicates the presence of a reversible redox partner

247   beyond Ir^{4+}/Ir$^{5.5+}$.

248   In addition to this high-voltage redox partner, the average and local structural behavior of LISO

249   differs from that of LIO. As first demonstrated by McCalla *et al.*,[15] a substantial degree of cation

250   site disorder develops in LISO after first delithiation. Figure 3b quantifies the extent of site

251   disorder in LISO25 before and after electrochemical cycling with either a 4.25 or 4.60 V cutoff.

252   The iterative Rietveld refinement results are shown in Fig. S10 and tables S3 & S4. As shown

253   schematically in Fig. 3b, we assume that each in-plane and out-of-plane antisite defect results in

254   a corresponding vacant M site (V_M). Since low concentrations of Sn_{Li} and Ir_{Li} have an identical

255   effect on the Bragg peak intensity, XRD cannot be used to differentiate between the migrating

256   species. We therefore perform the refinement assuming either all Ir_{Li} for both in-plane and out-

257   of-plane defects or only Sn_{Li} for out-of-plane defects and Ir_{Li} for in-plane defects (assuming all

258   Sn_{Li} for both types of defect leads to full depletion of the Sn content in the M sites in LISO25).

259   We quantify the total amount of disorder by the fraction of V_M, which reaches between

260   8.97±0.9% (assuming all Ir_{Li} defects) and 12.0±1.4 % (assuming Sn_{Li} for out-of-plane defects

261   and Ir_{Li} for in-plane defects) after a single cycle between 4.60-2.50 V, approximately evenly split

262   between in-plane and out-of-plane antisite defects. Since the total accessed capacity is

263   approximately the same between LIO and the various LISO compositions, by substituting with

264   Sn we can conclude that the structural disordering is not due to global structural instability

265   caused by low lithium contents. Instead, the disordering appears to be associated with the new

266   redox partner giving rise to the high voltage plateau: the disorder in LISO25 after a full cycle is

267   dramatically greater than in both LIO after the first cycle and LISO25 after a single cycle

268   between 4.25-2.50 V, which are both zero within experimental error. Out-of-plane refinement of

269   the fully charged O1 structure shows that the disorder is increased substantially at 4.60 V (tables

270   S3 & S4), providing a direct connection between the new redox partner, electrochemical

271   irreversibility, and the onset of cation disordering. Increased cation disordering with increased

272   redox capacity beyond $Ir^{4+/5.5+}$ is further supported by pair distribution function (PDF) analysis

273   (figs. S11-S14 and table S5) and EXAFS at the Ir L_3 edge (Fig. S15), which shows that the

274   decrease in scattering intensity of the first and second coordination shells during charge in LISO

275   – indicative of disorder in the atomic distances – is more substantial when the fraction of

276   capacity beyond $Ir^{4+/5.5+}$ is greater (i.e. with increasing Sn content). The changes to the XRD

277   pattern in charged LISO50 (Fig. S16) are complex and make reliable quantification of

278   occupancies with Rietveld refinement challenging. However, refinement in the discharged state

279   (tables S6 & S7) and the PDF and EXAFS behavior are similar to, and show more extensive

280   disordering than, LISO25. As discussed later, DFT also consistently predicts more favorable in-

281   plane and out-of-plane cation migration in fully charged LISO compared to LIO, further

282   supporting cation disordering during charge.

283

O redox switched on by Sn substitution

285   The electrochemical and structural data confirm that Sn substitution turns on an additional high

286   voltage redox partner that is associated with M_{Li}/V_M defect formation and voltage hysteresis. To

287   further probe the nature of the high voltage LISO redox partner, we perform *operando*

288   transmission XAS at the Ir L_3 and Sn K edges and RIXS at the O K edge. Figures 3c and S17a

289   show that, as with LIO, charging to 4.25 V results in a shift to higher energy of the Ir L_3 WL

290   energy. This is correlated with an increase in intensity of the Ir $5d$-O $2p$ t_{2g} peak at the O K edge

291   (Fig. 3d), confirming that this is standard hybridized Ir–O redox. Strikingly, the Ir L_3 WL energy

292   is essentially unchanged when charging beyond 4.25 V, exhibiting only a slight decrease in the

293   peak intensity (Fig. S17c). As argued previously, the invariance of the Ir L_3 WL is indicative of a

294   constant oxidation state and thus we rule out continued hybridized Ir-O redox during the high

295   voltage plateau. Figure S17d shows that the Sn K edge absorption changes minimally during

296   charge in LISO25, ruling out the improbable scenario of Sn oxidation beyond 4+.

297   The constant Ir/Sn oxidation states during the high voltage plateau suggest O redox, and we

298   again turn to the O K edge XAS/RIXS for confirmation. Figure 3d shows that when charging

299   LISO25 from 4.25 to 4.60 V, the t_{2g} peak continues to increase in intensity despite the invariance

300   of the Ir L_3 edge WL. This indicates an increased O $2p$ character in the t_{2g} band without the

301   depopulation of hybridized Ir–O states. Additionally, Fig. 3e shows that when charging to 4.60

13

302   V, a sharp RIXS feature at 530.7 eV excitation energy and 523.0 eV emission energy (indicated

303   by the white arrows) emerges. This is seen more clearly in the RIXS emission spectra in Fig. 3f.

304   The feature is strongest in LISO50, which exhibits the greatest extent of high-voltage capacity

305   beyond $Ir^{4+/5.5+}$ (Fig. 3a) and antisite/vacancy defects. This RIXS feature has been observed to

306   closely follow oxygen redox activity in several battery electrodes.[6, 31] Both of these behaviors

307   indicate that, in addition to promoting cation disordering, Sn substitution in LISO also switches

308   on O redox.

309

310   **Cation migration and O redox stabilized by LMCT *via* short Ir–O π bonding and O–O**

311   **dimerization**

312   Understanding why Sn substitution gives rise to these phenomena is central to uncovering the

313   origin of the coupling between anion redox and metal migration/vacancy formation. Since the

314   defect concentration is more reliably quantified in LISO25, we focus our DFT analysis on this

315   composition. First, we show in Fig. S18 the evolution of the computed DOS in the control case

316   of ordered, M_{Li}/V_M-free LISO25 as a function of Li stoichiometry. We observe that no

317   unhybridized O *2p* states are depopulated in the fully delithiated O1 structures – only hybridized

318   Ir–O states are accessed, giving Ir a formal oxidation state of at least 6+, which is inconsistent

319   with our XAS results. In fact, the behavior is similar to LIO (albeit more oxidized), with the

320   unhybrdizied O 2p states positioned ~1 eV below the Fermi level. Thus, simple delithiation and

321   the O3-O1 stacking change does not explain the high voltage redox process in LISO.

322   Importantly, our DFT calculations suggest that O redox *cannot* occur in LISO after delithiating

323   1.5 Li per formula unit if M_{Li}/V_M defects are not allowed to form.

324 Next, we introduce the experimentally-observed Sn_{Li}/V_M defects and examine their effect on the

325 electronic structure and charge distribution of LISO. Out-of-plane Sn migration into a Li layer

326 site creates a cation vacancy, V_M, and neighboring single-coordinate (dangling) oxygen atoms

327 (Fig. S19). Note that we use the term "single-coordinate" to refer to the number of covalent

328 bonding partners – i.e. counting Ir or Sn, but not Li. We find the formation of Sn_{Li}/V_M defect

329 pairs stabilizes the delithiated structure significantly by 1.34-1.36 eV, whereas the formation of

330 Ir_{Li}/V_M defect pairs is predicted to have a much smaller driving force of 0.02 eV.

331 We attribute the Sn_{Li}/V_M stabilization to the response of the resulting M-O dangling bonds,

332 which undergo one of two major transformations. As shown in Fig. 4a, when M = Ir, these bonds

333 contract substantially, changing from ~2.10 Å to ~1.77 Å. Figure 4b shows that the bond

334 contraction accompanies a splitting of the previously unhybridized O $2p$ states (shaded, top

335 panel), with some states moving above the Fermi level and becoming oxidized (shaded, bottom

336 panel). The shifted states, now approximately 1.5 eV higher in energy, rehybridize with the Ir $5d$

337 states. Table S8 shows that the bond contraction results in a donation of charge from the

338 dangling oxygens to the Ir bonding partners. Crystal orbital overlap population (COOP) analysis

339 in Supplementary discussion S4 and Fig. S20 shows that the net bond order between the dangling

340 O and Ir ions increases by 45 % as a result. Together, these observations suggest the formation of

341 short Ir–O π bonds (equivalently, terminal oxo ligands) through donation of oxygen lone pair

342 electrons, approaching Ir=O double bonds although an exact bond order is hard to define in an

343 electronically delocalized crystal. Indeed the substantially shortened Ir–O bonds (1.76 – 1.79 Å)

344 are similar in length to the Ir=O double bond observed in tetrahedral oxotrimesityliridium(V).[34]

345 While short Ir–O π bonding in octahedral environments has not been previously observed in

346   molecular compounds, the low effective Ir^{6+} d count (d^3) makes such bonding possible in

347   charged LISO.[35]

348   When M = Sn, on the other hand, the single-coordinate oxygens are predicted to instead pair up

349   to form short (~ 1.44 Å) O–O dimers that straddle the V_M (Fig. 4c and Fig. S19). Again, this

350   transformation results in a shift of the previously buried NB O $2p$ states from below to above the

351   Fermi level (Fig. 4d) along with donation of electron density from O to a neighboring Ir (table

352   S9). We stress that these localized dimers are distinct from the long (~ 2.5 Å) dimers previously

353   proposed for this material[15] in that they are well within the range of typical bond lengths for O_2^{n-}

354   species[33] and, crucially, do not form in the absence of cation migration. These behaviors – the

355   stabilization of the charged structure through Sn migration and Ir=O/O–O formation – are also

356   predicted for LISO50 (Fig. S21). We furthermore note that the computational conclusions are

357   independent of the functional employed (table S10).

358   We note that when both oxygens neighboring the V_M are coordinated to an Ir ion, the short Ir–O

359   π bonds are generally predicted to be more favored than O-O dimers (Fig. S21 and table S10).

360   However, as the Sn content is increased, the fraction of Sn-Sn neighbors increases and thus so

361   does the fraction of Sn-coordinated dangling oxygens after TM migration/vacancy formation,

362   which favor O–O formation (Fig. S21 and table S11). This observation may be due to the

363   increased rotational freedom of the Sn–O bond, facilitating O–O dimerization,[5] as well as the

364   ability of TMs with low d counts (such as $Ir^{5+/6+}$) to adopt terminal oxo ligands in octahedral

365   environments.[35] In addition, in-plane M_{Li}/V_M defect pairs can give rise to the same behavior (Fig.

366   S22).

367   Both the V_M-mediated O–O dimer and short Ir–O bond models are consistent with the local

368   structural evolution measured through EXAFS and PDF. EXAFS (Fig. S15) shows a substantial

369   decrease in the Ir–O scattering intensity during charge in LISO, which is exacerbated with

370   increasing oxygen redox capacity, consistent with an increased range of Ir–O bond lengths.

371   Meanwhile PDF (Fig. S14) shows a broadening of the M–O nearest neighbor scattering peak in

372   charged LISO, with an increase in scattering intensity at lower radial distance, consistent with

373   the formation of bonds shorter than the octahedral M–O distance of ~ 2 Å.

374   Additionally, both the O–O dimer and short Ir–O bond mechanisms are supported by the

375   spectroscopy data. Figure 4b predicts the donation of the buried O $2p$ electrons to the over-

376   oxidized Ir ions by raising these buried states above the Fermi level and into the t_{2g} band,

377   preventing Ir from exceeding the 5.5+ oxidation state. This is consistent with the increase in the

378   O K edge t_{2g} peak intensity (Fig. 3d) in the absence of a shift in the Ir L_3 WL energy during

379   oxygen redox (Fig. 3c). Meanwhile, the sharp RIXS feature is associated with specific

380   excitations in highly oxidized states, especially those involving unoccupied O $2p$ states in

381   oxidized oxygen species. Both peroxides[36] and O_2 gas[37] display the same kind of RIXS feature as

382   do charged Li-rich $3d$ layered oxides.[4, 6, 16, 31] Consistently, the formation of O–O dimers presents

383   a mechanism through which the buried O $2p$ states may become unoccupied during delithiation

384   in LISO. While our proposal of O-O is consistent with the RIXS result, we cannot rule out the

385   possibility that different types of oxidized oxygen species may also give rise to a similar feature.

386   Under our earlier definition, the formation of O_2^{2-} dimers qualifies as oxygen redox since, as

387   shown in Fig. 4, O $2p$ states are shifted above the Fermi level (i.e. depopulated) and end up as

388   the peroxide σ^*, which has mostly oxygen character. Thus, this mechanism serves to localize

389   positive charge onto O $2p$ orbitals even in an otherwise highly covalent system. However, in the

390   case of forming short Ir–O π bonds, while the O 2p states are again shifted above the Fermi level,

391   they end up rehybridizing with Ir t_{2g} states. In this case, although this results in additional

392   capacity beyond $Ir^{4+/5.5+}$, the character of these states, and thus the extent to which this counts as

393   oxygen redox, depends on the TM–O hybridization. While the hybridization may be significant

394   in the LISO materials, the nature of such states could be different in less covalent materials, such

395   as $3d$ TM oxides, and could therefore be important for oxygen redox in other systems.

396   To understand why LISO undergoes cation migration and oxygen redox while LIO does not, we

397   show in Supplementary discussion S5 that the driving force for forming Sn_{Li}/V_M defect pairs

398   depends strongly on the electron count in LISO, becoming favorable only when this falls below

399   1.5 e^- per Ir less than that of the pristine material. Thus, it is clear that the driving force for this

400   structure-redox coupling in LISO is the over-oxidation of Ir beyond an average 5.5+ oxidation

401   state. It is also clear that in the two structural transformations described in Fig. 4 (Ir=O and O–O)

402   substantial donation of charge occurs from O to Ir. It has been shown that in Na-ion battery

403   compounds unusually high oxidation states such as Fe^{4+} and Cu^{3+} are stabilized by LMCT,

404   wherein a substantial donation of charge from oxygen to the metal center occurs through strong

405   M–O covalency and low charge transfer energy.[38] We therefore propose that when oxidizing

406   beyond $Ir^{5.5+}$ a sufficiently low charge transfer energy is achieved such that substantial LMCT is

407   promoted and, consequently, new structural motifs and bonding configurations that allow for

408   greater LMCT become stabilized. In the case of Ir=O, the Ir–O bond length is substantially

409   shortened such that the covalency and LMCT is increased (as is clear in figs. 4b and S20 and is

410   well known, for example, for the Mn=O bonds in $KMnO_4$[39]), while in the case of O–O electrons

411   are directly transferred from the O–O σ* to neighboring Ir ions. Figure 5 shows the stepwise

412   process schematically: over-oxidation of Ir through delithiation, followed by Sn migration to

413   create either Ir=O or O–O species with a resulting donation of charge back to Ir, with the net

414   result being oxidation of O. Since the predicted O–O dimer bond length is 1.44 Å, we depict

415 these dimers as peroxide species in Fig. 5. Since the average Ir oxidation state never exceeds

416 5.5+ in LIO, substantial LMCT is not promoted, and therefore LIO exhibits excellent retention of

417 its in-plane and out-of-plane cation order during cycling and no anion redox.

418 Thus, the single-coordinate oxygens simultaneously stabilize both the low valence electron count

419 in charged LISO through LMCT and the resulting oxidized oxygen species, whether they settle

420 as terminal oxo ligands or O–O dimers. Consequently, they promote and stabilize the formation

421 of Sn_{Li}/V_M defects. Importantly, this structure-redox coupling quantitatively accounts for the

422 anion redox capacity. The diffraction results give a V_M concentration in LISO25 of 12.0±1.4%

423 assuming out-of-plane Sn_{Li} defects and in-plane Ir_{Li} defects. This extent of disordering is

424 accompanied by an additional redox capacity of ~0.48 Li beyond $Ir^{4+/5.5+}$. Assuming each

425 decoordinated oxygen contributes one redox electron, this implies that on average ~ 4 oxidized

426 oxygens are generated per migrated atom. Each in-plane and out-of-plane migration pathway

427 studied here generates 4 dangling oxygens, in agreement with this value.

428 We note that the spectroscopic and structural signature of oxidized oxygen in LISO is strikingly

429 similar to that in *3d* and *4d* Li-rich layered oxides.[6, 31] Further work is needed to establish the

430 precise commonalities between 3*d*, 4*d*, and 5*d* Li-rich electrode materials, in particular the

431 mechanism of decoordination and the relative driving force for forming short M–O π bonds

432 versus short ~ 1.44 Å O–O dimers. However, this initially suggests that depopulation of the high-

433 energy O *2p* states lying along the linear Li-O-Li axes of the honeycomb environments in Li-rich

434 layered oxides is generally stabilized through antisite/vacancy formation, short M–O π bonding,

435 and/or short O–O dimerization. Indeed, ab initio molecular dynamics studies have predicted such

436 mechanisms in *3d* Li-rich materials.[40] This also means that the same two-M-coordinate Li-O-Li

437 environments (where M is a covalent, non-alkali cation) that promote oxygen redox by raising

438   the energy of the O $2p$ states also facilitate its stabilization, as only a single M-Li site swap is

439   required to reach single-M-coordinate. In systems such as LISO where these O $2p$ states are not

440   sufficiently high lying to be depopulated in the disorder-free state, O redox can still occur if the

441   valence electron count is depleted low enough for substantial LMCT to be promoted via the

442   formation of antisite/vacancy defects, donating the otherwise inaccessible O $2p$ electrons to a

443   TM to form the resulting M-O π bonds and O–O dimers.

444   This mechanism contrasts with the conventional thinking that antisite/vacancy formation in Li-

445   rich layered oxides is driven by the destabilization of the layered structure at low Li

446   stoichiometries.[15, 41, 42] We instead propose that this defect behavior is best understood as an

447   overall decoordination of oxygen in response to low valence electron counts and/or oxygen

448   redox. Indeed, this explains why the onset of electrochemical irreversibility for wide a range of

449   Sn content coincides with exceeding the $Ir^{5.5+}$ oxidation state and not a specific Li stoichiometry

450   (Fig. 3a). We also emphasize that this decoordination takes the form of both in-plane and out-of-

451   plane cation disorder. This rationalizes early theories of Li-rich layered oxide structural behavior,

452   which proposed a conversion of the honeycomb superstructure to a layered $LiMO_2$ phase via in-

453   plane cation migration,[43] with later studies observing out-of-plane site disorder creating spinel-

454   like structures.[41]

455

456   **Conclusion**

457   In summary, by investigating the effect of Sn substitution in the LIO/LISO model system, we

458   have revealed the origin of the strong coupling between anion redox and structural disordering in

459   Li-rich layered oxides that underlies their irreversible electrochemical properties. We find that

460   LIO exhibits no anion redox, and multivalent hybridized Ir–O redox accounts for the entire

20

461   capacity, reconciling why this material exhibits more reversible electrochemical and structural

462   behavior than most known anion-redox-active Li-ion electrode materials. Thus, the long ~ 2.5 Å

463   O–O "dimers" that form in LIO during charge are not evidence of anion redox. When Sn is

464   substituted, the lower valence electron count towards the end of charge promotes substantial

465   LMCT through the formation of short Ir–O π bonds and ~ 1.4 Å O–O dimers, requiring the

466   presence of neighboring cation vacancies and therefore driving the formation of Sn_{Li}/V_M defect

467   pairs. The LMCT realized by the Ir=O and O–O species maintains Ir at its maximum oxidation

468   state of 5.5+ and results, on balance, in O redox. The spectroscopic and structural similarities

469   between O redox in LISO and a range of other Li-rich layered oxides[6, 31, 44] suggest that oxygen

470   redox may be generally stabilized in the local coordination environments created through local

471   structural defects. Although further study is needed to establish the commonalities between

472   materials, this explanation rationalizes the widespread coupling of oxygen redox to cation

473   disordering that gives rise to its irreversible electrochemical properties.

474   We expect that the nature of the TM=O and O–O species, along with the kinetics and

475   thermodynamics of forming the M_{Li}/V_M defect pair will determine the materials' voltage, long

476   term cycling stability, and rate capability, offering a new framework in which to optimize the

477   performance of Li-rich electrodes. We further suggest that structures outside the layered $Li_{1+x}M_{1-}$

478    $_xO_2$ framework that can accommodate the formation of short O–O and/or TM=O bonds through

479   small distortions rather than substantial cation rearrangement or, alternatively, materials that can

480   achieve substantial LMCT without drastic structural changes (e.g. through enhanced covalency)

481   could exhibit improved electrochemical and structural reversibility during anion redox. Indeed,

482   in Na-ion layered oxides where interlayer cation migration is limited and possibly even

483   prevented by the large interlayer spacing and/or prismatic interlayer site geometry, structurally

484   reversible anion redox can be achieved.[45, 46] Given the stabilizing effect of cation migration

485   demonstrated here, the relative reactivity of these materials towards the electrolyte and oxygen

486   evolution in the absence of cation migration will be an interesting avenue of further study. Our

487   results reveal a clear strategy for designing materials for applications beyond energy storage

488   where low valence electron counts (high oxidation states) need to be reversibly accessed, such as

489   catalysts for reactions including oxygen evolution,[20, 47, 48] olefin polymerization,[49] and methane

490   hydroxylation.[50]

491

References

492

493   1.   Whittingham MS. Ultimate Limits to Intercalation Reactions for Lithium Batteries.
494   *Chemical Reviews* 2014, **114**(23)**:** 11414-11443.
495   2.   Assat G, Tarascon J-M. Fundamental understanding and practical challenges of anionic
496   redox activity in Li-ion batteries. *Nature Energy* 2018, **3**(5)**:** 373-386.
497   3.   Sathiya M, Rousse G, Ramesha K, Laisa CP, Vezin H, Sougrati MT, *et al.* Reversible
498   anionic redox chemistry in high-capacity layered-oxide electrodes. *Nature Materials*
499   2013, **12:** 827.
500   4.   Luo K, Roberts MR, Hao R, Guerrini N, Pickup DM, Liu Y-S, *et al.* Charge-
501   compensation in *3d*-transition-metal-oxide intercalation cathodes through the generation
502   of localized electron holes on oxygen. *Nature Chemistry* 2016, **8:** 684.
503   5.   Seo D-H, Lee J, Urban A, Malik R, Kang S, Ceder G. The structural and chemical origin
504   of the oxygen redox activity in layered and cation-disordered Li-excess cathode materials.
505   *Nature Chemistry* 2016, **8:** 692.
506   6.   Gent WE, Lim K, Liang Y, Li Q, Barnes T, Ahn S-J, *et al.* Coupling between oxygen
507   redox and cation migration explains unusual electrochemistry in lithium-rich layered
508   oxides. *Nature Communications* 2017, **8**(1)**:** 2091.
509   7.   Zhan C, Yao Z, Lu J, Ma L, Maroni VA, Li L, *et al.* Enabling the high capacity of
510   lithium-rich anti-fluorite lithium iron oxide by simultaneous anionic and cationic redox.
511   *Nature Energy* 2017, **2**(12)**:** 963-971.
512   8.   Assat G, Delacourt C, Corte DAD, Tarascon J-M. Editors' Choice—Practical Assessment
513   of Anionic Redox in Li-Rich Layered Oxide Cathodes: A Mixed Blessing for High
514   Energy Li-Ion Batteries. *Journal of The Electrochemical Society* 2016, **163**(14)**:** A2965-
515   A2976.
516   9.   Sathiya M, Abakumov AM, Foix D, Rousse G, Ramesha K, Saubanère M, *et al.* Origin of
517   voltage decay in high-capacity layered oxide electrodes. *Nature Materials* 2014, **14:** 230.
518   10.   Dogan F, Long BR, Croy JR, Gallagher KG, Iddir H, Russell JT, *et al.* Re-entrant lithium
519   local environments and defect driven electrochemistry of Li- and Mn-rich Li-ion battery
520   cathodes. *Journal of the American Chemical Society* 2015, **137**(6)**:** 2328-2335.
521   11.   Croy JR, Gallagher KG, Balasubramanian M, Chen Z, Ren Y, Kim D, *et al.* Examining
522   hysteresis in composite xLi$_2$MnO$_3$·(1–x)LiMO$_2$ cathode structures. *The Journal of*
523   *Physical Chemistry C* 2013, **117**(13)**:** 6525-6536.
524   12.   Kleiner K, Strehle B, Baker AR, Day SJ, Tang CC, Buchberger I, *et al.* Origin of High
525   Capacity and Poor Cycling Stability of Li-Rich Layered Oxides: A Long-Duration in Situ
526   Synchrotron Powder Diffraction Study. *Chemistry of Materials* 2018, **30**(11)**:** 3656-3667.
527   13.   Abdellahi A, Urban A, Dacek S, Ceder G. The effect of cation disorder on the average Li
528   intercalation voltage of transition-metal oxides. *Chemistry of Materials* 2016, **28**(11)**:**
529   3659-3665.
530   14.   Konishi H, Hirano T, Takamatsu D, Gunji A, Feng X, Furutsuki S, *et al.* Potential
531   hysteresis between charge and discharge reactions in Li$_{1.2}$Ni$_{0.13}$Mn$_{0.54}$Co$_{0.13}$O$_2$ for lithium
532   ion batteries. *Solid State Ionics* 2017, **300:** 120-127.
533   15.   McCalla E, Abakumov AM, Saubanère M, Foix D, Berg EJ, Rousse G, *et al.*
534   Visualization of O-O peroxo-like dimers in high-capacity layered oxides for Li-ion
535   batteries. *Science* 2015, **350**(6267)**:** 1516-1521.
536   16.   Luo K, Roberts MR, Guerrini N, Tapia-Ruiz N, Hao R, Massel F, *et al.* Anion redox

chemistry in the cobalt free *3d* transition metal oxide intercalation electrode Li[Li$_{0.2}$Ni$_{0.2}$Mn$_{0.6}$]O$_2$. *Journal of the American Chemical Society* 2016, **138**(35)**:** 11211-11218.

17.   Kobayashi H, Tabuchi M, Shikano M, Kageyama H, Kanno R. Structure, and magnetic and electrochemical properties of layered oxides, Li$_2$IrO$_3$. *Journal of Materials Chemistry* 2003, **13**(4)**:** 957-962.

18.   Delmas C, Braconnier J-J, Fouassier C, Hagenmuller P. Electrochemical intercalation of sodium in Na$_x$CoO$_2$ bronzes. *Solid State Ionics* 1981, **3-4**(Supplement C)**:** 165-169.

19.   Perez AJ, Jacquet Q, Batuk D, Iadecola A, Saubanère M, Rousse G*, et al.* Approaching the limits of cationic and anionic electrochemical activity with the Li-rich layered rocksalt Li$_3$IrO$_4$. *Nature Energy* 2017, **2**(12)**:** 954-962.

20.   Grimaud A, Hong WT, Shao-Horn Y, Tarascon JM. Anionic redox processes for electrochemical devices. *Nature Materials* 2016, **15:** 121.

21.   Yabuuchi N, Nakayama M, Takeuchi M, Komaba S, Hashimoto Y, Mukai T*, et al.* Origin of stabilization and destabilization in solid-state redox reaction of oxide ions for lithium-ion batteries. *Nature Communications* 2016, **7:** 13814.

22.   Choy J-H, Kim D-K, Hwang S-H, Demazeau G, Jung D-Y. XANES and EXAFS Studies on the Ir-O Bond Covalency in Ionic Iridium Perovskites. *Journal of the American Chemical Society* 1995, **117**(33)**:** 8557-8566.

23.   Mugavero SJ, Smith MD, Yoon W-S, zur Loye H-C. Nd$_2$K$_2$IrO$_7$ and Sm$_2$K$_2$IrO$_7$: Iridium(VI) oxides prepared under ambient pressure. *Angewandte Chemie International Edition* 2009, **48**(1)**:** 215-218.

24.   Laguna-Marco MA, Kayser P, Alonso JA, Martínez-Lope MJ, van Veenendaal M, Choi Y*, et al.* Electronic structure, local magnetism, and spin-orbit effects of Ir(IV)-, Ir(V)-, and Ir(VI)-based compounds. *Physical Review B* 2015, **91**(21)**:** 214433.

25.   Qi B, Perez I, Ansari PH, Lu F, Croft M. *L$_2$* and *L$_3$* measurements of transition-metal *5d* orbital occupancy, spin-orbit effects, and chemical bonding. *Physical Review B* 1987, **36**(5)**:** 2972-2975.

26.   Yoon W-S, Balasubramanian M, Chung KY, Yang X-Q, McBreen J, Grey CP*, et al.* Investigation of the charge compensation mechanism on the electrochemically Li-ion deintercalated Li$_{1-x}$Co$_{1/3}$Ni$_{1/3}$Mn$_{1/3}$O$_2$ electrode system by combination of soft and hard X-ray absorption spectroscopy. *Journal of the American Chemical Society* 2005, **127**(49)**:** 17479-17487.

27.   Mortemard de Boisse B, Liu G, Ma J, Nishimura S-i, Chung S-C, Kiuchi H*, et al.* Intermediate honeycomb ordering to trigger oxygen redox chemistry in layered battery electrode. *Nature Communications* 2016, **7:** 11397.

28.   Qiao R, Wray LA, Kim J-H, Pieczonka NPW, Harris SJ, Yang W. Direct Experimental Probe of the Ni(II)/Ni(III)/Ni(IV) Redox Evolution in LiNi$_{0.5}$Mn$_{1.5}$O$_4$ Electrodes. *The Journal of Physical Chemistry C* 2015, **119**(49)**:** 27228-27233.

29.   Liu X, Wang YJ, Barbiellini B, Hafiz H, Basak S, Liu J*, et al.* Why LiFePO$_4$ is a safe battery electrode: Coulomb repulsion induced electron-state reshuffling upon lithiation. *Physical Chemistry Chemical Physics* 2015, **17**(39)**:** 26369-26377.

30.   Maitra U, House RA, Somerville JW, Tapia-Ruiz N, Lozano JG, Guerrini N*, et al.* Oxygen redox chemistry without excess alkali-metal ions in Na$_{2/3}$[Mg$_{0.28}$Mn$_{0.72}$]O$_2$. *Nature Chemistry* 2018.

31.   Xu J, Sun M, Qiao R, Renfrew SE, Ma L, Wu T*, et al.* Elucidating anionic oxygen

activity in lithium-rich layered oxides. *Nature Communications* 2018, **9**(1)**:** 947.

32. Chen H, Islam MS. Lithium Extraction Mechanism in Li-Rich Li_2MnO_3 Involving Oxygen Hole Formation and Dimerization. *Chemistry of Materials* 2016, **28**(18)**:** 6656-6663.

33. Cramer CJ, Tolman WB, Theopold KH, Rheingold AL. Variable character of O—O and M—O bonding in side-on (η^2) 1:1 metal complexes of O_2. *Proceedings of the National Academy of Sciences* 2003, **100**(7)**:** 3635-3640.

34. Hay-Motherwell RS, Wilkinson G, Hussain-Bates B, Hursthouse MB. Synthesis and X-ray crystal structure of oxotrimesityliridium(V). *Polyhedron* 1993, **12**(16)**:** 2009-2012.

35. Winkler JR, Gray HB. Electronic Structures of Oxo-Metal Ions. In: Mingos DMP, Day P, Dahl JP (eds). *Molecular Electronic Structures of Transition Metal Complexes I*. Springer Berlin Heidelberg: Berlin, Heidelberg, 2012, pp 17-28.

36. Zhuo Z, Pemmaraju CD, Vinson J, Jia C, Moritz B, Lee I, *et al.* Spectroscopic Signature of Oxidized Oxygen States in Peroxides. *The Journal of Physical Chemistry Letters* 2018, **9**(21)**:** 6378-6384.

37. Hennies F, Pietzsch A, Berglund M, Föhlisch A, Schmitt T, Strocov V, *et al.* Resonant Inelastic Scattering Spectra of Free Molecules with Vibrational Resolution. *Physical Review Letters* 2010, **104**(19)**:** 193002.

38. Talaie E, Kim SY, Chen N, Nazar LF. Structural Evolution and Redox Processes Involved in the Electrochemical Cycling of P2–$Na_{0.67}[Mn_{0.66}Fe_{0.20}Cu_{0.14}]O_2$. *Chemistry of Materials* 2017, **29**(16)**:** 6684-6697.

39. Gilbert B, Frazer BH, Belz A, Conrad PG, Nealson KH, Haskel D, *et al.* Multiple Scattering Calculations of Bonding and X-ray Absorption Spectroscopy of Manganese Oxides. *The Journal of Physical Chemistry A* 2003, **107**(16)**:** 2839-2847.

40. Benedek R. First-cycle simulation for Li-rich layered oxide cathode material $xLi_2MnO_3 \cdot (1-x)LiMO_2$ (x = 0.4). *Journal of The Electrochemical Society* 2018, **165**(11)**:** A2667-A2674.

41. Mohanty D, Li J, Abraham DP, Huq A, Payzant EA, Wood DL, *et al.* Unraveling the Voltage-Fade Mechanism in High-Energy-Density Lithium-Ion Batteries: Origin of the Tetrahedral Cations for Spinel Conversion. *Chemistry of Materials* 2014, **26**(21)**:** 6272-6280.

42. Ceder G, Van der Ven A. Phase diagrams of lithium transition metal oxides: investigations from first principles. *Electrochimica Acta* 1999, **45**(1)**:** 131-150.

43. Thackeray MM, Kang S-H, Johnson CS, Vaughey JT, Benedek R, Hackney SA. Li_2MnO_3-stabilized $LiMO_2$ (M = Mn, Ni, Co) electrodes for lithium-ion batteries. *Journal of Materials Chemistry* 2007, **17**(30)**:** 3112-3125.

44. Okubo M, Yamada A. Molecular Orbital Principles of Oxygen-Redox Battery Electrodes. *ACS Applied Materials & Interfaces* 2017, **9**(42)**:** 36463-36472.

45. Mortemard de Boisse B, Nishimura S-i, Watanabe E, Lander L, Tsuchimoto A, Kikkawa J, *et al.* Highly reversible oxygen-redox chemistry at 4.1 V in $Na_{4/7-x}[\square_{1/7}Mn_{6/7}]O_2$ ($\square$: Mn Vacancy). *Advanced Energy Materials* 2018, **8**(20)**:** 1800409.

46. Rong X, Liu J, Hu E, Liu Y, Wang Y, Wu J, *et al.* Structure-induced reversible anionic redox activity in Na layered oxide cathode. *Joule* 2018, **2**(1)**:** 125-140.

47. Surendranath Y, Kanan MW, Nocera DG. Mechanistic Studies of the Oxygen Evolution Reaction by a Cobalt-Phosphate Catalyst at Neutral pH. *Journal of the American Chemical Society* 2010, **132**(46)**:** 16501-16509.

629   48.   Grimaud A, Diaz-Morales O, Han B, Hong WT, Lee Y-L, Giordano L*, et al.* Activating
630   lattice oxygen redox reactions in metal oxides to catalyse oxygen evolution. *Nature*
631   *Chemistry* 2017, **9:** 457.

632   49.   Billow BS, McDaniel TJ, Odom AL. Quantifying ligand effects in high-oxidation-state
633   metal catalysis. *Nature Chemistry* 2017, **9:** 837.

634   50.   Snyder BER, Vanelderen P, Bols ML, Hallaert SD, Böttger LH, Ungur L*, et al.* The active
635   site of low-temperature methane hydroxylation in iron-containing zeolites. *Nature* 2016,
636   **536:** 317.

637

638

639
640

641 **Methods**

642 <u>Materials</u>

643   Li_2IrO_3 (hereafter, LIO), $Li_2Ir_{0.75}Sn_{0.25}O_3$ (hereafter, LISO25), and $Li_2Ir_{0.5}Sn_{0.5}O_3$ (hereafter,

644   LISO50) were synthesized by solid state reactions. Appropriate amounts of Li_2CO_3 (Alfa Aesar,

645   99.998% metal basis), IrO_2 (Alfa Aesar, 99.99% metals basis), and SnO_2 (Alfa Aesar 99.9%

646   metals basis) were mixed using a planetary ball mill. 10% excess amount of Li_2CO_3 was used to

647   compensate the lithium evaporation at high temperature. Mixed powder was heat treated at

648   1000 °C for 12 hours twice in a box furnace with an intermittent grinding, and then naturally

649   cooled to room temperature.

650

651 <u>Electrochemical measurements and electrode harvesting</u>

652   For all electrochemistry figures in this study, 80 wt. % active material, 10 wt.%

653   polyvinylidene fluoride (PVDF) binder (MTI Corporation) and 10 wt. % carbon black (Timcal

654   C65) were mixed with N-methyl-2-pyrrolidone (Acros Organics) and the slurry was cast onto

655   carbon-coated Al foil using a doctor blade. The electrode sheet was dried at 110 °C in air for 1 h

656   followed by overnight at 60 °C under vacuum. Coin cells (CR2032, Wellcos Corporation) were

657   assembled in an Ar filled glove box with a ~11.3 mm diameter LIO/LISO electrode, two 25 µm

658   thick Celgard separators, a 750 µm thick Li foil counter electrode (Sigma-Aldrich), and 1 M

659    $LiPF_6$ in 1:1 (v/v) ethylene carbonate (EC)/diethyl carbonate (DEC) electrolyte (Selectilyte LP

660   40, BASF). The coin cells were cycled under a constant current density of a C/12 rate (1C = 211

661   mA g$^{-1}_{LIO}$, 227.4 mA g$^{-1}_{LISO25}$, 246.6 mA g$^{-1}_{LISO50}$ corresponding to the (de)lithiation rate of 2Li/h

662   f.u.) between 4.60 V and 2.50 V (LIO and LISO) or 4.25 V and 2.50 V (LISO). Galvanostatic

663   intermittent titration technique (GITT) was applied to measure the open circuit voltage (OCV) at

664   various states of charge and the thermodynamic voltage hysteresis of LIO and LISO. We applied

665   constant current pulses (C/20) for an hour followed by the relaxation for four hours. This was

666   repeated until the GITT cycle was complete.

667   *Ex situ* soft XAS (fluorescence yield), X-ray diffraction (XRD), and resonant inelastic X-

668   ray scattering (RIXS) samples were dismantled from coin cells at the indicated states of charge

669   in an Ar filled glove box. Cells were dismantled using a coin cell decrimping instrument (MTI

670   Corporation). The electrodes were then rinsed with excess DEC and dried under vacuum in the

671   glove box antechamber. For XRD, materials were scraped off of the Al foil current collector and

672   then sealed in a glass capillary (0.5 mm diameter, Ted Pella). All the samples were transferred to

673   the desired instrument in a double-sealed Al-coated polypropylene pouch to prevent air exposure.

674

675   <u>X-ray diffraction and Rietveld refinement</u>

676   High resolution powder XRD patterns for Rietveld refinement were measured at beamline

677   2-1 at the Stanford Synchrotron Radiation Lightsource (SSRL, SLAC National Accelerator

678   Laboratory) at 17 keV (0.7293 Å) beam energy for as-synthesized powders and at beamline 11-

679   ID-B at the Advanced Photon Source (APS, Argonne National Laboratory) at 58.4 keV (0.2114

680   Å) beam energy for *ex situ* samples scraped out of electrodes after electrochemical cycling. The

681   size of the X-ray beam was 500 x 1500 μm (SSRL) or 500 x 500 μm (APS). All of the samples

682   were prepared in capillaries to avoid possible preferred orientation of the particles. All of the

683   samples were measured using the transmission geometry.

684   We used the TOPAS software package (Academic v6, Bruker) for Rietveld refinement.

685   Pawley fitting was employed to determine the crystallographic parameters. The pristine and the

686   samples fully charged to 4.60 V were refined with the *C2/m* space group following previous

687 reports.[15] For the T3-Li$_1$IrO$_3$, we found the *Cm* space group to give the best results. For LISO, we

688 assumed that Ir and Sn are randomly distributed through the 4h sites in the TM layer, and the

689 migrated Ir/Sn from 4h was assumed to redistribute equally to the 4g and 2c sites in the Li layer.

690 We allowed variations in the Ir occupancy in Li layer of the fully charged (4.60 V) and fully

691 discharged (2.50 V) LIO and confirmed no Ir migration during the first cycle in LIO.

692

693 X-ray total scattering and pair-distribution function analysis

694 Atomic pair-distribution function (PDF) was analyzed to gain further insights on the local

695 atomic structures of LIO and LISO of the pristine powder and the samples scraped out of the

696 electrodes charged to 4.60 V and discharged to 2.50 V. X-ray total scattering was collected at

697 beamline 11-ID-B at the APS at 58.4 keV (0.2114 Å) beam energy. All of the samples were

698 packed in Kapton capillaries double sealed in Al-coated pouch in an argon filled glove box, and

699 then transferred to the beamline. The pouch was opened right before the measurement to

700 minimize the air exposure. The data collection time was three minutes per sample. We used

701 PDFgetX2 to obtain the atomic PDF from the total scattering data and PDFGUI to fit the atomic

702 PDF from the starting crystal structures determined by Rietveld refinement described above.

703

704 *Operando* Ir L$_3$ edge XAS and EXAFS spectroscopy

705 For *operando* X-ray absorption spectroscopy (XAS), Al-coated poly propylene (PP) pouch

706 cells containing a ~11.3 mm diameter LIO/LISO electrode, two 25 μm thick Celgard separators,

707 a 250 μm thick Li foil counter electrode (Alfa Aesar), and 1 M LiPF$_6$ in 1:1 (v/v) ethylene

708 carbonate (EC)/diethyl carbonate (DEC) electrolyte (Selectilyte LP 40, BASF), a Ni negative

709 current collector tab, and an Al positive current collector tab were assembled using a tabletop

710   vacuum impulse sealer (Fuji Impulse) in an argon filled glove box. A stainless steel holder with a

711   pair of Be plates (Ted Pella) as an X-ray window was machined to apply a sufficient pressure on

712   the pouch cells using torque screws. The pressure from the stiff windows significantly improved

713   electronic conduction throughout the micro-porous electrodes ensuring homogeneity. The pouch

714   cells were cycled using a portable potentiostat (SP-150, Biologic) under a constant current

715   density of C/12 (where 1C refers to 2Li/h f.u.) between 4.60 V and 2.50 V (*vs.* Li) with 1 hr rest

716   between charge and discharge.

717   The Ir L3 edge XAS spectra of LIO and LISO was collected at beamline 2-2 of Stanford

718   Synchrotron Radiation Lightsource (SSRL) at SLAC National Accelerator Laboratory and

719   beamline 20-BM of the Advanced Photon Source (APS) at Argonne National Laboratory,

720   respectively. The transmission spectra were measured using a 1 x 7 mm unfocused X-ray beam.

721   A Si (220) (SSRL) or Si (111) (APS) crystal monochromator was detuned to 70% of its original

722   intensity to eliminate high order harmonics. Three ion chambers filled with N_2 gas were used in

723   series to simultaneously measure I_0, I_1, and I_{ref}. A Ge reference foil was used to calibrate the

724   photon energy by setting the peak of the first derivative of the K edge absorbance spectrum to be

725   11102 eV. 10 eV, 0.5 eV, and 10 eV energy steps were used in the ranges of 10985-11085 eV,

726   11085.5-11124.5 eV, and 11125-11195 eV, respectively, in order to precisely measure the

727   reference Ge K edge spectra for the calibration followed by the Ir L_3 edge measurement. We

728   used the Athena software package to align and normalize the collected spectra. White line peak

729   was fitted using the sum of an error function and a Lorentzian peak analogous to previous reports.

730   Fourier transformations of k^2 weighted extended X-ray absorption fine-structure (EXAFS)

731   spectra were carried out in the k range from 2 $Å^{-1}$ to 14 $Å^{-1}$ for all the materials.

732

733

<u>O K edge Soft X-ray Absorption Spectroscopy: FY, RIXS, and transmission</u>

734

735   O K edge sXAS of the harvested electrodes were measured in fluorescence yield (FY) mode

736   at SSRL beam line 10-1 equipped with a silicon photodiode detector (AXUV100). Data was

737   acquired under ultrahigh vacuum (10^{-9} Torr) at room temperature with the incident X-ray beam

738   of 500 μm x 500 μm size.

739   RIXS maps were collected at beam line 8.0.1 at the Advanced Light Source (ALS) in

740   Lawrence Berkeley National Laboratory, using the ultrahigh efficiency iRIXS endstation. All the

741   harvested electrodes were sealed in Al pouches in an argon filled glove box and transferred into a

742   specially designed transfer kit and then the experimental vacuum chamber to avoid air exposure.

743   Technical details of the RIXS beam line and data processing can be found in our previous

744   reports.[6, 51] Two-dimensional emission spectra collected at each excitation energy are aligned

745   using the elastic peak and a reference compound such as TiO_2 to generate the full RIXS maps.

746   The color scale has been tuned in the figures to emphasize the contrast of intensity.

747   Transmission O K edge sXAS was measured at ALS beam line 11.0.2 using Scanning

748   Transmission X-ray Microscopy. The samples were prepared by sonicating the harvested

749   electrodes in dimethyl carbonate under argon for two hours at room temperature to separate

750   individual particles out of the composite electrodes. The particle suspension was drop-cast onto

751   copper TEM grids with a carbon film (Ted Pella). The grids were loaded onto a sample holder,

752   sealed in an Al-coated pouch, and then transferred to the beam line. We first collected the STXM

753   images with a 50 nm zone plate, an interferometer-controlled stage, and a point detector. The

754   step size was 50 nm and the dwell time for each pixel was typically 1 ms. STXM spectro-images

755   were aligned in the aXis2000 software package. To obtain average absorption spectra, the

756 aligned absorbance images were filtered at an energy of non-zero intensity, typically 529.5 eV.

757 The pixels below a threshold intensity were set to zero. The remaining un-normalized pixels

758 were then summed to yield the average spectrum. For presentation, normalization of the average

759 spectra was done by subtracting the background intensity and then dividing by the post edge

760 intensity.

761

762 <u>Computational details</u>

763 The calculations for all structures presented were performed with density functional theory

764 (DFT) as implemented in the Vienna *Ab-initio* Simulation Package (VASP).[52, 53] Valence

765 electrons were described by the plane wave basis set and core electrons were incorporated by the

766 projector augmented-wave method.[54-57] Unless otherwise indicated, the perdew-burke-ernzerhof

767 (PBE) functional[58] with the Hubbard U correction[59] was adopted for the exchange correlation

768 energy. An effective U value of 2.75 eV was applied on Ir.[60] For hybrid calculations, the HSE

769 screened coulomb hybrid density functional[61] was used with a mixing parameter of 0.15 and a

770 range separation parameter of 0.2.[62] The energy cutoff of the plane wave basis was 520 eV and

771 the k-point mesh was $3 \times 3 \times 7$ for a $2 \times 2 \times 1$ supercell of O3-$Li_{2-x}MO_3$. Van der Waals

772 interactions were taken into account using the D2 method of Grimme[63] for PBE+U and HSE

773 calculations. For SCAN calculations, the rVV10 non-local van der Waals correlation functional

774 was used.[64] To prepare the structures of $Li_{2-x}IrO_3$, we generated all Li-vacancy orderings within

775 the unit cell of $Li_{2-x}IrO_3$ including 4 formula units using the enumeration technique developed by

776 Hart *et al*.[65, 66] and 10 configurations at x = 1.5 and 0.5 and 100 configurations at x = 1 with

777 lowest electrostatic energy were calculated using GGA. The configurations with the lowest

778 DFT/GGA energy at each Li content were selected as most stable structures. Both octahedral and

32

779 tetrahedral sites in Li layer within O3- and O1-Li_xIrO_3 were considered for Li-vacancy orderings

780 at x=1. The same Li-vacancy orderings were applied to the $Li_{2-x}Ir_{0.75}Sn_{0.25}O_3$ case. After Sn

781 migration to Li layer, the Li-vacancy orderings were re-sampled using the basin hopping

782 algorithm.[67]

783

784 **Data Availability**

785 All experimental data within the article and its Supplementary Information will be made

786 available upon reasonable request to the authors.

787

788 **References**

789 51. Chuang Y-D, Shao Y-C, Cruz A, Hanzel K, Brown A, Frano A, *et al.* Modular soft x-ray
790 spectrometer for applications in energy sciences and quantum materials. *Review of*
791 *Scientific Instruments* 2017, **88**(1)**:** 013110.
792 52. Kresse G, Hafner J. *Ab initio* Moleculare Dynamics for Liquid Metals. *Physical Review B*
793 1993, **47**(1)**:** 558-561.
794 53. Kresse G, Hafner J. *Ab initio* Molecular-dynamics Simulation of the Liquid-metal
795 Amorphous-semiconductor Transition in Germanium. *Physical Review B* 1994, **49**(20)**:**
796 14251-14269.
797 54. Kresse G, Furthmüller J. Efficient iterative schemes for ab initio total-energy calculations
798 using a plane-wave basis set. *Physical Review B* 1996, **54**(16)**:** 11169-11186.
799 55. Kresse G, Furthmüller J. Efficiency of ab-initio total energy calculations for metals and
800 semiconductors using a plane-wave basis set. *Computational Materials Science* 1996,
801 **6**(1)**:** 15-50.
802 56. Blöchl PE. Projector augmented-wave method. *Physical Review B* 1994, **50**(24)**:** 17953-
803 17979.
804 57. Kresse G, Joubert D. From ultrasoft pseudopotentials to the projector augmented-wave
805 method. *Physical Review B* 1999, **59**(3)**:** 1758-1775.
806 58. Perdew JP, Burke K, Ernzerhof M. Generalized gradient approximation made simple.
807 *Physical Review Letters* 1996, **77**(18)**:** 3865-3868.
808 59. Dudarev SL, Botton GA, Savrasov SY, Humphreys CJ, Sutton AP. Electron-energy-loss
809 spectra and the structural stability of nickel oxide: An LSDA+U study. *Physical Review B*
810 1998, **57**(3)**:** 1505-1509.
811 60. Subedi A. First-principles study of the electronic structure and magnetism of $CaIrO_3$.

812   *Physical Review B* 2012, **85**(2)**:** 020408.

813   61.   Heyd J, Scuseria GE, Ernzerhof M. Hybrid functionals based on a screened Coulomb
814   potential. *The Journal of Chemical Physics* 2003, **118**(18)**:** 8207-8215.

815   62.   Seo D-H, Urban A, Ceder G. Calibrating transition-metal energy levels and oxygen bands
816   in first-principles calculations: Accurate prediction of redox potentials and charge transfer
817   in lithium transition-metal oxides. *Physical Review B* 2015, **92**(11)**:** 115118.

818   63.   Grimme S. Semiempirical GGA-type density functional constructed with a long-range
819   dispersion correction. *Journal of Computational Chemistry* 2006, **27**(15)**:** 1787-1799.

820   64.   Peng H, Yang Z-H, Perdew JP, Sun J. Versatile van der Waals Density Functional Based
821   on a Meta-Generalized Gradient Approximation. *Physical Review X* 2016, **6**(4)**:** 041005.

822   65.   Hart GLW, Forcade RW. Algorithm for generating derivative structures. *Physical Review
823   B* 2008, **77**(22)**:** 224115.

824   66.   Hart GLW, Nelson LJ, Forcade RW. Generating derivative structures at a fixed
825   concentration. *Computational Materials Science* 2012, **59:** 101-107.

826   67.   Wales DJ, Doye JPK. Global optimization by basin-hopping and the lowest energy
827   structures of Lennard-Jones clusters containing up to 110 atoms. *The Journal of Physical
828   Chemistry A* 1997, **101**(28)**:** 5111-5116.

829

830

854

Author Contributions: J.H., W.E.G., W.C.C, and M.F.T. conceived the study. J.H. carried out materials synthesis, characterization and testing. J.H. and K.L. performed ex situ and *operando* synchrotron measurements including XRD, PDF, XAS, sXAS, and RIXS. J.H. and W.E.G. measured ex situ STXM and RIXS spectra. W.E.G., J.W., and W.Y. processed and analyzed spectroscopic data. K.L., J.H., K.H.S., D.Passarello, and M.F.T. performed the structural analyses. K.L., J.H., C.J.T., M.F.T. and W.C.C. designed and constructed settings for in situ synchrotron measurements. P.X., D.-H.S., and G.C. conducted DFT calculations. J.W., K.H.S., D.N., C.S., and K.H. configured synchrotron end stations. P.M.C. provided constructive advice for experiments. J.H., W.E.G., D.Prendergast, W.C.C, and M.F.T. devised the oxygen redox model. J.H., W.E.G., G.C., W.C.C., and M.F.T. wrote the manuscript and all authors revised the manuscript.

866

868

869
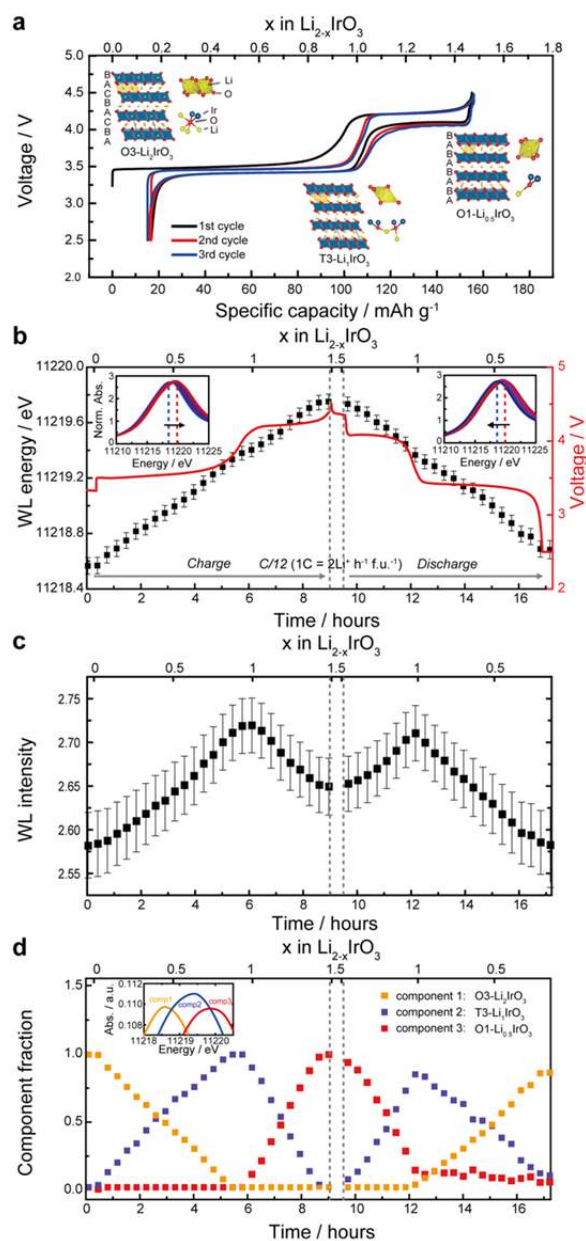
Fig. 1. Reversible multivalent iridium redox in Li$_{2-x}$IrO$_3$. (a) Capacity-voltage curves of Li$_2$-$_x$IrO$_3$ galvanostatically measured at a C/12 rate (17.58 mA g^{-1}) between 4.50-2.50 V for the initial three cycles. The stable phases during the two consecutive two-phase reactions of Li$_{2-x}$IrO$_3$ occurring at each voltage plateau, obtained by combined XRD Rietveld refinements and DFT calculations, are shown. **(b)** Evolution of the Ir L$_3$ WL energy (black squares) during the first

875   cycle, measured through *operando* transmission XAS, showing the continuous

876   oxidation/reduction of iridium throughout the whole charge/discharge processes. Error (see

877   methods) was determined to be reasonably small. The raw XANES data for charging and

878   discharging are shown in the left and right insets, respectively. (**c**) Evolution of the Ir L_3 WL

879   intensity, showing the largest intensity at the Li_1IrO_3 composition, where Ir is in the 5+ oxidation

880   state. It is known that Ir^{5+} has a higher WL intensity than Ir^{4+} and Ir^{6+}[23, 24] and thus the

881   subsequent intensity decay is consistent with further oxidation of Ir^{5+} to $Ir^{5.5+}$ during the high

882   voltage plateau at 4.15 V. (**d**) LCA of NMF components, showing three distinct Ir L_3-edge

883   spectra as end members (inset).

884

885
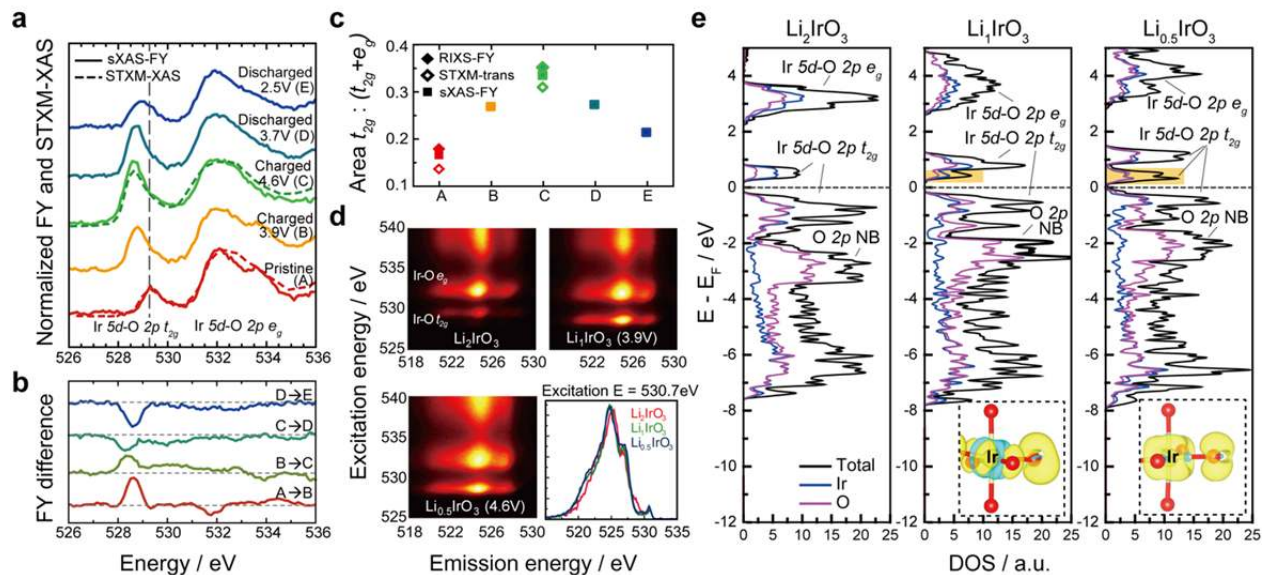
Fig. 2. **Hybridized Ir-O redox in Li$_{2-x}$IrO$_3$**. (**a**) sXAS fluorescence yield spectra (solid lines)

and XAS obtained through scanning transmission X-ray microscopy (STXM-XAS, dashed lines)

of the O K edge of Li$_{2-x}$IrO$_3$ at various voltages throughout the first cycle. From bottom to top,

pristine (red, A), charged to 3.9 V (yellow, B), charged to 4.6 V (green, C), discharged to 3.7 V

after being charged to 4.6 V (olive, D), discharged to 2.5 V after being charged to 4.6 V (blue,

E). (**b**) Difference plot of sXAS obtained from (a) showing the intensity evolution of Ir *5d* -O *2p*

t$_{2g}$ and e$_g$* peaks. (**c**) Ratio of the Ir *5d*-O *2p* t$_{2g}$ peak area to the total Ir *5d*-O *2p* t$_{2g}$ + e_g* area

measured by RIXS, STXM and sXAS, showing the continuous growth and decay of the t$_{2g}$ area.

The O K edge measurements were normalized by the intensity at 545 eV after subtracting the

background intensity. (**d**) O K edge RIXS maps of Li$_2$IrO$_3$, LiIrO$_3$ and Li$_{0.5}$IrO$_3$. The right

bottom panel shows the RIXS spectra at 530.7 eV excitation energy for each composition where

a feature corresponding to anion redox is reported to appear. (**e**) Ir- and O-projected density of

states of Li$_2$IrO$_3$, LiIrO$_3$ and Li$_{0.5}$IrO$_3$ calculated from first principles, demonstrating no access to

the buried O *2p* non-bonding states. Insets show the isosurface of the charge density for the

900   lowest unoccupied states corresponding to 0.5 electrons/f.u. in $LiIrO_3$ and $Li_{0.5}IrO_3$ (shaded

901   region in (e)) visualizing two different Ir *5d*-O *2p* t_{2g} hybridized states. Yellow and blue show

902   negative and positive changes in charge density, respectively. Li ions are omitted for clarity.

903
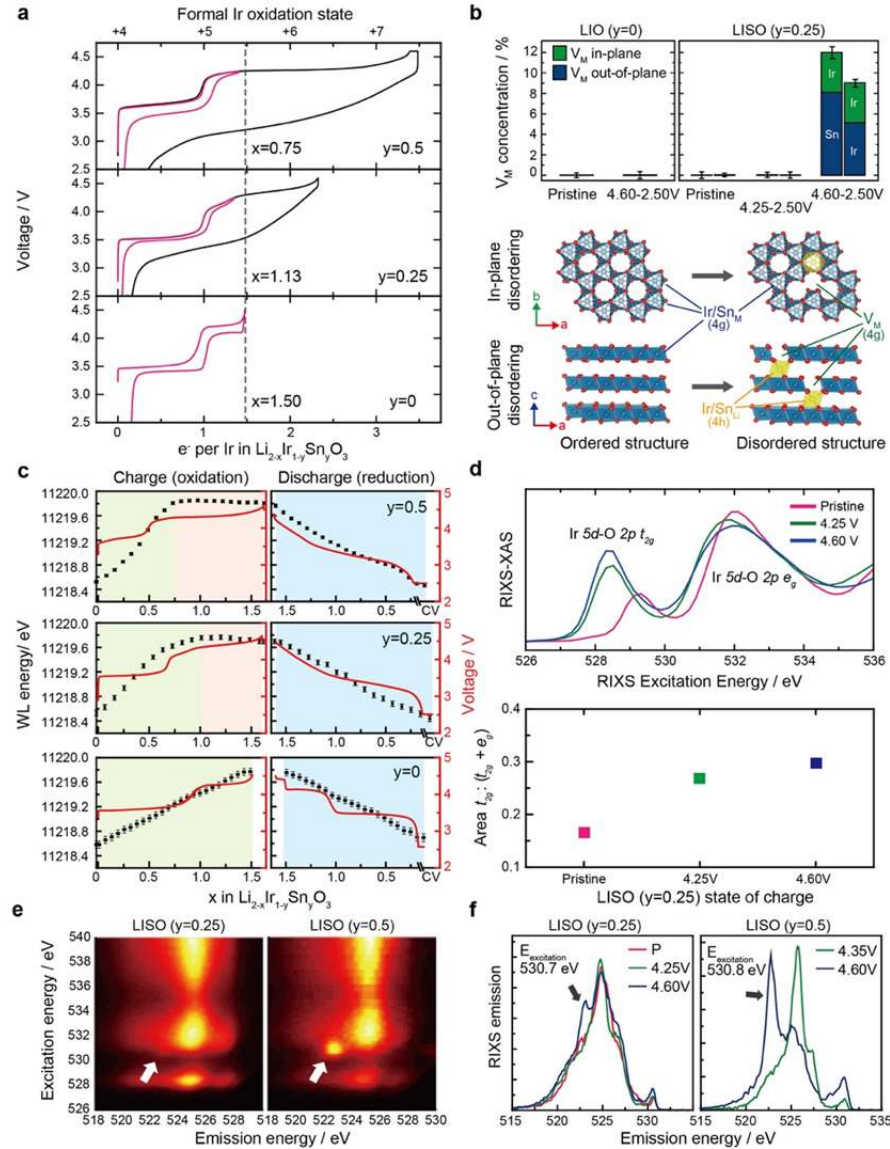
Fig. 3. **Irreversible electrochemistry, structural disordering, and redox behavior of Li$_{2-x}$Ir$_{1-y}$Sn$_y$O$_3$.** (**a**) Charge/discharge profiles of Li$_{2-x}Ir_{1-y}Sn_yO_3$ (y=0, 0.25, 0.5) under a constant current density (C/10 rate) for a full cycle (black) and for an approximately 1.5 electron per Ir per f.u. cycle (pink). (**b**) In-plane and out-of-plane disorder quantified by iterative XRD Rietveld refinement for the LISO25 cycled in the 4.60-2.50 V and 4.25-2.50 V windows and LIO cycled in the 4.60-2.50 V window, quantified by the total V$_M$ concentration. The scheme illustrates the

911   in-plane (top) and out-of-plane (bottom) structural disordering mechanisms resulting in V_M, with

912   the migrated cation octahedron shaded yellow and the Wyckoff positions indicated in

913   parentheses. (**c**) *Operando* transmission XANES spectra of the Ir L_3 edge for the first cycle

914   showing the continuous Ir oxidation up to 4.25 V, no shift beyond 4.25 V, and the continuous Ir

915   reduction during discharge. (**d**) FY sXAS O K edge spectra (obtained by integrating the RIXS

916   data onto the excitation axis, RIXS-XAS) throughout the first cycle for LISO25 (top) and the

917   corresponding ratio of the Ir *5d*-O *2p* t_{2g} peak area to the total Ir *5d*-O *2p* $t_{2g} + e_g^*$ area (bottom).

918   (**e**) O K edge RIXS maps of LISO25 (left) and LISO50 (right) charged to 4.60 V showing a

919   localized RIXS feature at 530.7 eV excitation energy and 522.8 eV emission energy. (**f**) Single

920   energy RIXS spectra of LISO25 and LISO50 more clearly showing the anion redox signature.

921

922
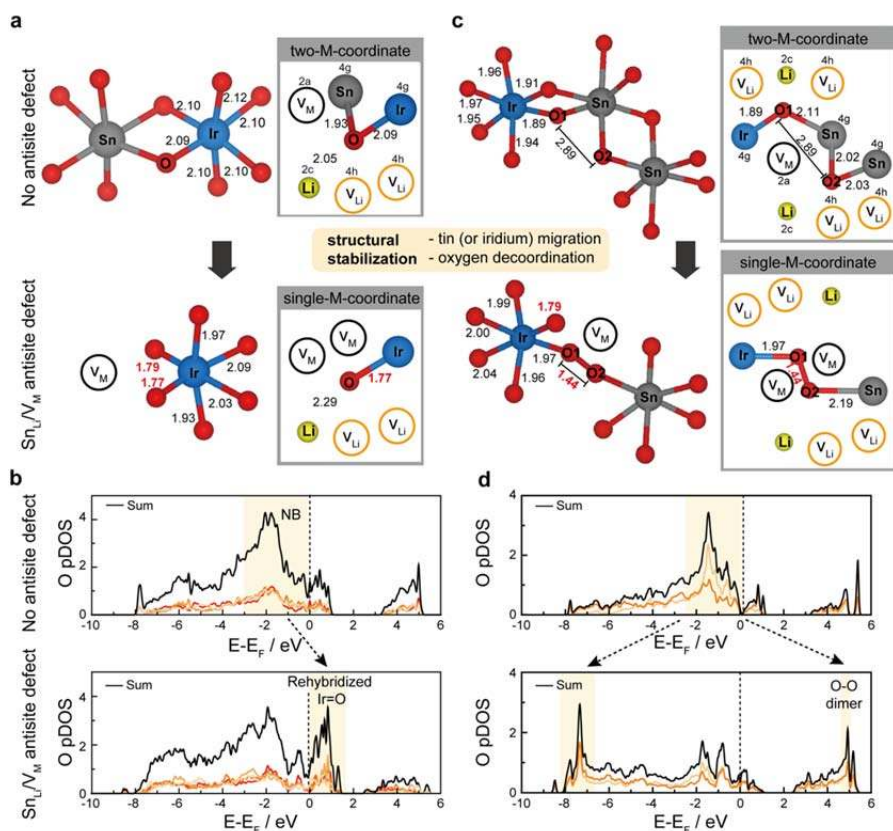
Fig. 4. Computational predictions of M-O decoordination and Ir=O/O–O stabilized anion redox. (**a**) Ir–O bond lengths (left) and oxygen coordination environments (right) predicted by DFT in a $Li_{0.5}Ir_{0.75}Sn_{0.25}O_3$ structure before (top) and after (bottom) the formation of a Sn_{Li}/V_M defect when the vacancy neighbors only Ir. Note that the presence of Li neighboring O negligibly affects the O $2p$ states due to minimal hybridization between Li and O. (**b**) Projected DOS of the individual oxygen atoms involved in the Ir–O bond contraction before (top) and after (bottom) forming the Sn_{Li}/V_M defect, demonstrating the shift of the O $2p$ states above the Fermi level, indicating oxygen redox. (**c**) Ir–O bond lengths (left) and oxygen coordination environments (right) before (top) and after (bottom) the formation of a Sn_{Li}/V_M defect when the migrating Sn initially neighbors another Sn, resulting in the formation of a 1.44 Å O–O dimer. (**d**) Projected DOS of the individual oxygen atoms involved in the O–O bond formation before (top) and after

43

934   (bottom) forming the Sn_{Li}/V_M defect and O–O dimer, also showing a shift of the O $2p$ states

935   above the Fermi level.

936

937
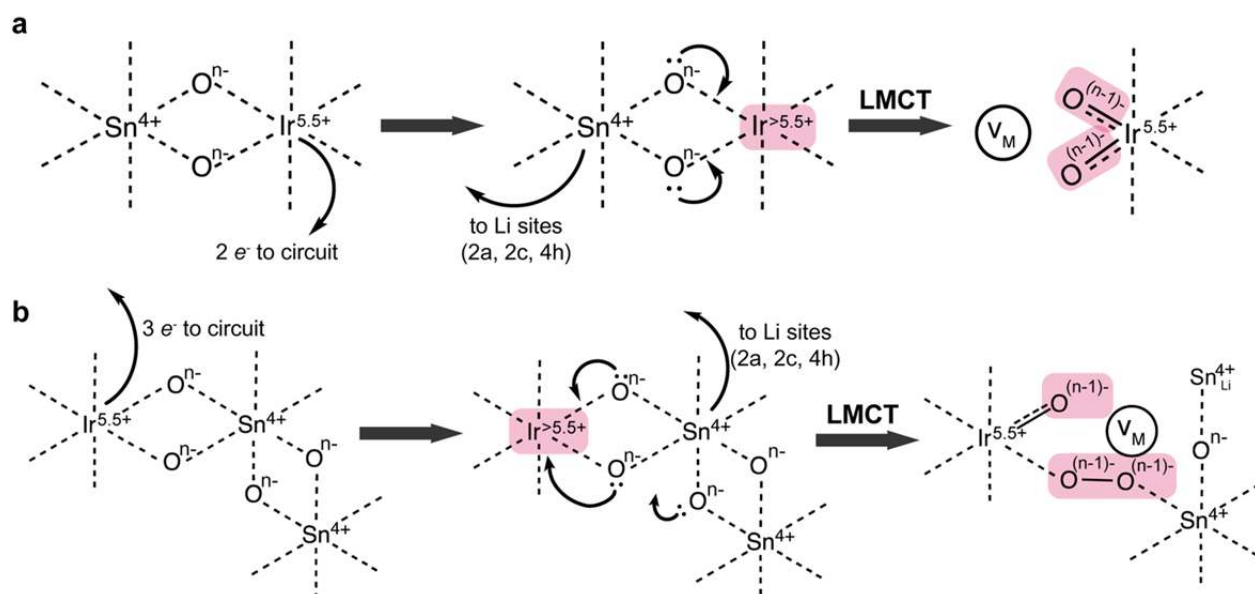
Fig. 5. **Proposed electronic mechanism of cation migration and LMCT mediated anion redox in LISO.** (**a**) The mechanism of Ir=O formation, wherein Ir is initially oxidized beyond $Ir^{5.5+}$, promoting LMCT *via* Sn migration, oxygen decoordination, and donation of oxygen lone pair (unhybridized O $2p$) electrons to forming a short Ir–O π bond. Each black arrow corresponds to the redistribution of an electron pair. **(b)** The mechanism of O–O formation when a dangling O is coordinated to a Sn atom, wherein LMCT is achieved instead through donation of the O–O σ^* electrons to Ir. Both cases assume that the number of electrons provided through LMCT mediated oxygen redox is equal to the number of decoordinated oxygens. Note that the calculations in Fig. 4 reflect only the LMCT step in both cases.